



Article

Self-assembly of anthraquinone covalent organic frameworks as 1D superstructures for highly efficient CO₂ electroreduction to CH₄

Ming Liu^{a,1}, Yi-Rong Wang^{a,1}, Hui-Min Ding^{a,1}, Meng Lu^a, Guang-Kuo Gao^a, Long-Zhang Dong^a, Qi Li^a, Yifa Chen^{a,b,*}, Shun-Li Li^a, Ya-Qian Lan^{a,b,*}

^aJiangsu Collaborative Innovation Centre of Biomedical Functional Materials, Jiangsu Key Laboratory of New Power Batteries, School of Chemistry and Materials Science, Nanjing Normal University, Nanjing 210023, China

^bSchool of Chemistry, South China Normal University, Guangzhou 510006, China

ARTICLE INFO

Article history:

Received 23 March 2021

Received in revised form 21 April 2021

Accepted 26 April 2021

Available online 5 May 2021

Keywords:

Covalent organic frameworks

1D superstructures

Nanofibers

Hollow tubes

CO₂ electroreduction

ABSTRACT

The design of selective and efficient covalent organic frameworks (COFs) based electrocatalysts with tunable morphology for efficient CO₂ reduction reaction (CO₂RR) to CH₄ is highly desirable. Here, two kinds of anthraquinone-based COFs (i.e., AAn-COF and OH-AAn-COF) with tunable 1D superstructures (e.g., nanofibers (NF) and hollow tubes (HT)) have been produced via Schiff-base condensation reaction. Interestingly, a rarely reported nanosheet-based self-template mechanism and a nanosheet-crimping mechanism have been demonstrated for the production of COF-based nanofibers and hollow tubes, respectively. Besides, the obtained COF-based superstructures can be post-modified with transition metals for efficient CO₂RR. Specifically, AAn-COF-Cu (NF) and OH-AAn-COF-Cu (HT) exhibit superior faradaic-efficiency with CH₄ (FE_{CH₄}) of 77% (−128.1 mA cm^{−2}, −0.9 V) and 61% (−99.5 mA cm^{−2}, −1.0 V) in a flow-cell, respectively. Noteworthy, the achieved FE_{CH₄} of AAn-COF-Cu (NF) (77%) is the highest one among reported crystalline COFs. This work provides a general methodology in exploring morphology-controlled COFs for electrocatalytic CO₂RR.

© 2021 Science China Press. Published by Elsevier B.V. and Science China Press. All rights reserved.

1. Introduction

Covalent organic frameworks (COFs), a kind of crystalline porous frameworks composed of non-metal elements (C, N, O, B, etc.), are connected and extended via stable covalent bonds [1]. Since the first introduction in 2005, COFs have evoked an immense level of recent interest around the world because of their advantageous nature like excellent crystallinity, permanent porosity, high thermal/chemical stability, low densities, tunable functionality and structures, etc. [2]. Thanks to the efforts of many groups, various COFs structures have been reported over the past decades, which have found interesting applications in energy storage [3], gas separation [4,5], proton conduction [6,7], sensing [8,9], drug delivery [10] and catalysis [11–14], etc. In view of the potential of using alternative materials in electrocatalytic CO₂RR, an elegant solution for renewable energy storage and closing the carbon cycle [13], is especially attractive owing to the following reasons: (1) the abundant channels are beneficial for CO₂ enrichment and mass transfer

to facilitate the contact between catalytic active centers and CO₂ [15]; (2) the functional structures endow COFs with functionality like electron donating/transferring or activation of CO₂ that might be beneficial for the performance improvement [15,16] and (3) the synthetic flexibility enables the introduction of various electroactive units or metal sites (e.g., Cu, Co, Ni, or Zn, etc.) through strategies like the incorporation of heteroatom, metalation, encapsulation of single sites or hybridization with other materials [13,17,18]. Besides, COFs with clear crystalline structures could provide a depth understanding of the structure–activity relationship in electrocatalysis, showing high promise in this field [13].

To date, COF-based materials for electrocatalytic CO₂RR have been intensively investigated during past decades and are mainly focused on porphyrin/phthalocyanine-based COFs and related derivatives [19–24]. Some pioneering COF-based structures such as porphyrin-based COFs like COF-366-Co and COF-367-Co [22], or phthalocyanine-based COFs like CoPc-PDQ-COF [19] and NiPc-COF [24] have been applied in electrocatalytic CO₂RR. Nevertheless, there are still some bottlenecks for COFs in this field: (1) most of the reduced products are two-electron transferred products like CO and the high-efficiency production of higher-value products (e.g., CH₄ and C₂H₄, etc.) involving multiple proton-coupled

* Corresponding authors.

E-mail addresses: chyf927821@163.com (Y. Chen), yqlan@m.scnu.edu.cn, yqlan@njnu.edu.cn (Y.-Q. Lan).

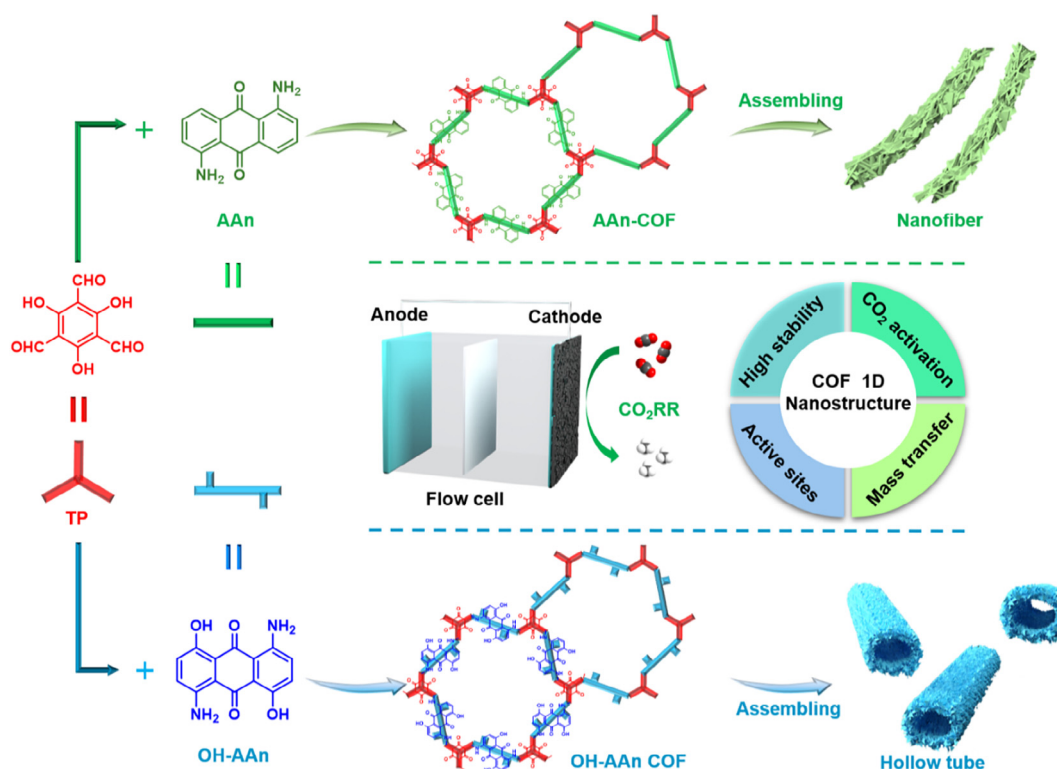
¹ These authors contributed equally to this work.

electron transfer (PCET) remains as a scientific challenge [19,22,25]; (2) the inert insulation nature of crystalline COFs has resulted in low conductivity and restricted the CO₂RR parameters like current density or product selectivity [20,25] and (3) competitive kinetically-favored H₂ generation reaction will lower the efficiency of desired products. Besides, closely packed COF structures, generally in eclipsed stacking fashion possessing π - π interaction, will be unfavorable for mass transfer and accessibility of the active sites, which might lead to low electrocatalytic performance [26–28]. Therefore, the exploration of morphology-controlled COFs with exposed active sites that enable the generation of higher-value products is highly valuable and urgently needed for the applications of COFs in electrocatalytic CO₂RR.

To this end, morphology-controlled strategies like “top-down” and “bottom-up” protocols have been proposed [26,28]. The “top-down” strategies like liquid phase exfoliation have been reported to transform bulk phases of COFs into lower-dimension forms like nanosheets, yet they are still limited by the entangled drawbacks like pre-synthesized COFs, tedious exfoliation processes, low yields, and inhomogeneity in the size or thickness [29,30]. In addition, “bottom-up” strategies including templated or template-free methods that enable simultaneous *in-situ* syntheses and morphology-control of COFs have been further explored [31,32]. In the reported template methods, COFs are firstly grown on the surface of templates (e.g., Fe₃O₄ and ZnO, etc.) with pre-designed morphologies (e.g., spherical or tubular shapes) followed by the removal of templates to produce shaped morphology [31,33]. However, they still face drawbacks like sophisticated template-removal processes. In contrast, template-free approaches are much more desired in both synthesis processing and morphology-control, in which COFs are firstly formed as small crystallites and then self-assembled into target morphology in the absence of templates [34–38]. Some pioneering works report that COFs can be self-assembled into various morphologies like nanosheets, spheres or fibers through the “bottom-up” template-

free strategies to investigate their potential applications in trypsin immobilization [35], energy storage [37] or guest molecule capture [38], etc. Nonetheless, the growth processing forms like 1D superstructures (e.g., NF or HT) are rare and the investigation of their formation mechanisms are still at the early stage [34,38,39]. Besides, it has been rarely reported that the application of morphology-controlled COF materials in electrocatalytic CO₂RR is studied. It would be highly important to investigate the influence of various morphologies on CO₂RR property and particularly attractive to explore the possibility of COF-based nanomaterials in selective production of multi-electron transferred products (e.g., CH₄ or C₂H₄, etc.).

Herein, two kinds of anthraquinone COFs (i.e., AAn-COF and OH-AAn-COF) with tunable 1D superstructures (e.g., NF and HT) have been synthesized and post-modified with various transition metals (e.g., Cu, Co, and Zn) to explore their CO₂RR performances (Scheme 1 and Fig. 1a). Interestingly, a rarely reported nanosheet-based self-template mechanism and a nanosheet-crimping mechanism have been revealed for COF-based nanofibers (NF) and hollow tubes (HT), respectively, as supported by time-interval experiments. The obtained anthraquinone COF-based nanostructures can serve as powerful electrocatalysts in CO₂RR, in which the porous nanostructures possess excellent chemical stability, large surface area, and CO₂ enrichment/activation ability, etc. Specifically, AAn-COF-Cu (NF) and OH-AAn-COF-Cu (HT) exhibit superior FE_{CH₄} of 77% (–0.9 V, –128.1 mA cm^{–2}) and 61% (–1.0 V, –99.5 mA cm^{–2}) in a flow-cell, respectively. Remarkably, the FE_{CH₄} of AAn-COF-Cu (NF) keeps higher than 53% over a wide potential range (–0.8 to –1.0 V) and the achieved FE_{CH₄} of 77% (–0.9 V) is the highest one among reported crystalline COFs in electrocatalytic CO₂RR. Besides, the effect of morphology on CO₂RR has been studied and the results show that the nanofiber morphology is more favorable for the production of CH₄ while hollow tube morphology has a particular control effect on the generation of ethylene. This is the first example of anthraquinone-based COFs



Scheme 1. (Color online) The schematic representation of anthraquinone COF-based nanofibers and hollow tubes in electrocatalytic CO₂RR.

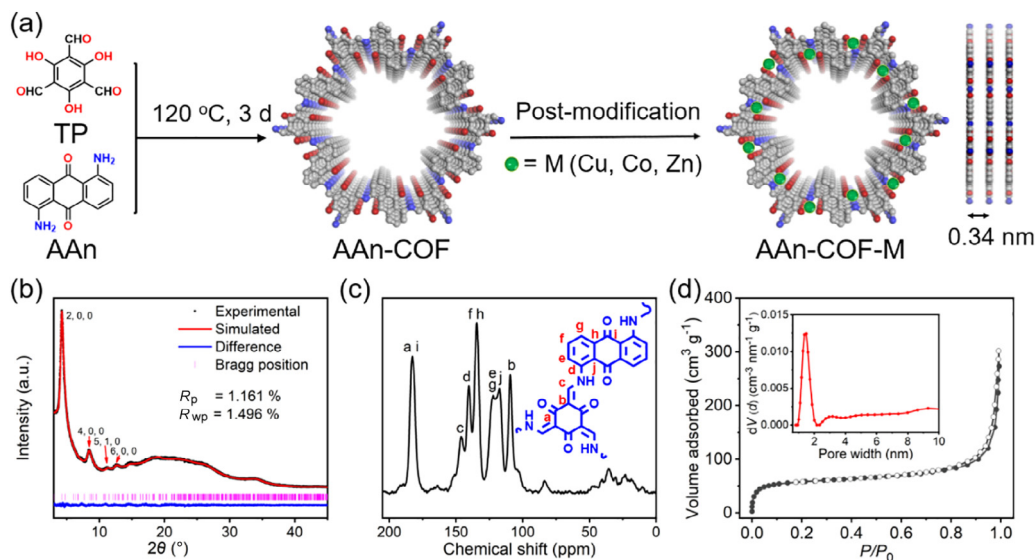


Fig. 1. (Color online) The structure and characterization of AAn-COF and AAn-COF-M ($M = \text{Cu, Co, Zn}$). (a) The schematic representation of the synthesis procedures of AAn-COF-M. (b) Experimental and simulated PXRD patterns of AAn-COF. (c) ^{13}C NMR spectrum of AAn-COF. (d) N_2 sorption curve of AAn-COF at 77 K (inset is pore-size distribution profile).

with unique and tunable 1D superstructures applied in efficient CO_2RR to CH_4 as far as we have known, which would expedite the development of COFs in this field.

2. Material and methods

2.1. Syntheses of samples

2.1.1. Preparation of 1,3,5-triformylphloroglucinol (TP)

TP was prepared based on the literature report with slight modification [40]. In detail, a uniformly ground mixture of hexamethylenetetramine (15.42 g, 0.11 mol) and anhydrous phloroglucinol (6.31 g, 0.05 mol) was mixed in a round bottom flask and the operation was conducted under N_2 atmosphere. Then, trifluoroacetic acid (100 mL) was added into the flask. The flask was heated at $100\text{ }^\circ\text{C}$ and kept stirring for 2.5 h, and then $\sim 160\text{ mL}$ 3 mol L^{-1} HCl was added and stirred for 1 h. When the temperature cools to room temperature (RT), the sample was filtered, and the product was extracted into dichloromethane ($3 \times 100\text{ mL}$). After that, the extracted organic solution was collected, dried with MgSO_4 and then filtered, and the solvent was removed through rotary evaporation to produce the crude product. Finally, the product was purified by washing with a large amount of hot ethanol to obtain a kind of light-yellow powder (1.3 g, 12.4% yield).

2.1.2. Preparation of AAn-COF

1,5-Diaminoanthraquinone (AAn, 21.5 mg, 0.09 mmol) and TP (12.4 mg, 0.04 mmol) were dissolved in the mixed solution of dioxane (0.25 mL), 1,3,5-trimethylbenzene (0.75 mL) and 6 mol L^{-1} acetic acid aqueous solution (AcOH, 0.3 mL) in a Pyrex tube (volume, 10 mL). After sonication for 15 min, the Pyrex tube was flash frozen at 77 K and degassed. After it recovered to RT, the Pyrex tube was treated at $120\text{ }^\circ\text{C}$ for 3 d. After that, the filtrated sample was added to a Soxhlet extractor and washed (tetrahydrofuran, 24 h and acetone, 24 h). Finally, the sample was heated at $120\text{ }^\circ\text{C}$ (under vacuum) for 12 h to produce an activated sample (29.1 mg, $\sim 86\%$ yield).

2.1.3. Preparation of OH-AAn-COF

The synthesis of OH-AAn-COF was based on previously reported reference with slight change [41]. 1,5-Diamino-4,8-dihydroxyanthraquinone (OH-AAn, 25.6 mg, 0.09 mmol) and TP (12.6 mg, 0.06 mmol) were dissolved in a mixed solution (0.4 mL dioxane, 0.8 mL 1, 2-dichlorobenzene and 0.2 mL 6 mol L^{-1} AcOH) in a Pyrex tube. After sonication for 15 min, the Pyrex tube was flash frozen at 77 K and degassed. After it recovered to RT, the Pyrex tube was treated at $120\text{ }^\circ\text{C}$ for 3 days. After that, the filtrated sample was added to a Soxhlet extractor and washed (tetrahydrofuran, 24 h and acetone, 24 h). Finally, the product was evacuated at $120\text{ }^\circ\text{C}$ under vacuum for 12 h to yield an activated sample (31.4 mg, $\sim 93\%$ yield).

2.1.4. Preparation of AAn-COF-Cu and OH-AAn-COF-Cu

AAn-COF-Cu and OH-AAn-COF-Cu were prepared through direct metallation of AAn-COF and OH-AAn-COF with $\text{Cu}(\text{OAc})_2 \cdot \text{H}_2\text{O}$. Taking AAn-COF-Cu as an example, AAn-COF (200 mg) was added in $\text{Cu}(\text{OAc})_2 \cdot \text{H}_2\text{O}$ (0.1 mol L^{-1} , 100 mL) solution followed with sonication for 5 min. The suspension was refluxed at $100\text{ }^\circ\text{C}$ for 72 h. After that, the sample was filtered and thoroughly washed with H_2O and ethanol each for three times. After drying at $100\text{ }^\circ\text{C}$ under vacuum for 12 h, the product was produced. The synthesis of OH-AAn-COF-Cu followed similar procedures.

2.1.5. Preparation of AAn-COF-Co and AAn-COF-Zn

The syntheses of AAn-COF-Co and AAn-COF-Zn followed the similar procedures of AAn-COF-Cu, except that $\text{Cu}(\text{OAc})_2 \cdot \text{H}_2\text{O}$ (0.1 mol L^{-1} , 100 mL) was replaced with $\text{Co}(\text{OAc})_2 \cdot 4\text{H}_2\text{O}$ and $\text{Zn}(\text{OAc})_2 \cdot 2\text{H}_2\text{O}$ in similar concentrations, respectively.

2.1.6. Syntheses of AAn-COF and OH-AAn-COF with different reaction time

The reaction mixture was added into several heat-resistant glass tubes followed similar treatment as mentioned above, and the individual samples were sequentially taken out of the oven after a specified time interval. After the different reaction time, the product was collected and dried in a similar manner. The obtained samples were characterized by powder X-ray diffraction (PXRD) and scanning electron microscopy (SEM) tests.

2.2. Material characterization

The PXRD spectra were tested on a D/max 2500 VL/PC X-ray diffractometer (Rigaku SmartLab, Japan) with Cu K α radiation ($\lambda = 1.5418 \text{ \AA}$) at 45 kV, 200 mA. Fourier transform infrared spectroscopy (FT-IR) was recorded on a Bruker Tensor 27 in the range of 4000–400 cm^{-1} . ^{13}C CP/MAS solid-state nuclear magnetic resonance (^{13}C NMR) spectra were measured by Bruker AVANCE III 400 spectrometer. Thermogravimetric analysis (TGA) tests were carried out on a Diamond TG/DTA/DSC Thermal Analyzer System (Perkin-Elmer, USA). N_2 and CO_2 sorption tests were conducted using a Micromeritics ASAP 2020 volumetric adsorption analyzer. Metal content analyses were obtained by inductively coupled plasma optic emission spectroscopy (ICP-OES) using Agilent 720ES. X-ray photoelectron spectroscopy (XPS) was tested by applying an Escalab 250Xi instrument (Thermo Scientific). Morphology study was performed with a field emission SEM (Quanta 250F). Transmission electron microscopy (TEM) images were conducted on a JEOL JEM-2100 electron microscope. Gas chromatography (GC) was performed on GC-7820A. The isotope-labeled experiment was performed using $^{13}\text{CO}_2$ instead of $^{12}\text{CO}_2$ and the result was analyzed by Gas chromatography-mass spectrometer (GC-MS, 7890B and 5977B, Agilent).

2.3. Structural modeling

The structural modeling was carried out in BIOVIA Materials Studio 2019 software and the theoretical models were optimized by the Forcite module. The Pawley refinement was conducted to iteratively optimize the lattice parameters. The profile fitting (e.g., peak asymmetry, peak broadening, and zero shift error, etc.) was treated with Pseudo-Voigt profile function until the R_{wp} and R_{p} values converge.

2.4. Electrochemical measurements

The electrolysis tests of the catalyst were performed in a flow cell at selected potentials to determine the CO_2 reduction activities. The working electrode was a gas diffusion layer (GDL) with catalyst coating. The counter and reference electrode were Pt foil and Ag/AgCl electrodes, respectively. Throughout all experiments, unless specially mentioned, 1 mol L^{-1} KOH electrolyte was flowed separately in cathode and anode chambers with a peristaltic pump (7 mL min^{-1}). Chronoamperometry was performed using an electrochemical workstation (SP-150, Bio-Logic) with a standard three-electrode system at RT. All potentials were tested versus Ag/AgCl electrode (with saturated KCl) with iR compensation, and the results were reported versus reversible hydrogen electrode (RHE) based on the Nernst equation: E (vs. RHE) = E (vs. Ag/AgCl) + 0.197 V + 0.059 \times pH. The gaseous reduction products (e.g., CO, CH_4 , C_2H_4 and H_2) were detected with a gas chromatography (Agilent 7820A). The electrolyte solution collected from the cathode chambers was applied to analyze the liquid products and characterized by ^1H nuclear magnetic resonance (^1H NMR, Bruker 500 MHz NMR instrument) (a mixture of 0.5 mL electrolyte and 0.1 mL D_2O). A solvent pre-saturation technique was applied to suppress the peak of water.

2.5. Preparation of working electrode

5 mg sample was grinded for 10 min and added in a mixed solution of ethanol (250 μL), water (200 μL) and Nafion solution (5 wt%, 50 μL). After sonication for 30 min, the 50 μL catalyst ink was directly spray-coated on a hydrophobic carbon paper to form a

$0.5 \times 1 \text{ cm}^2$ catalyst area with a $\sim 1 \text{ mg cm}^{-2}$ loading. The deposited carbon paper was further dried at RT.

3. Results and discussion

3.1. Structure and characterization of samples

AAn-COF and OH-AAn-COF are prepared by the Schiff base reaction of AAn and OH-AAn with TP, respectively (Scheme 1 and Fig. 1a). The structures of COFs are resolved by PXRD tests in conjunction with Pawley refinements and BIOVIA Materials Studio 2019 is applied for the structural simulations. Taking AAn-COF for example, AAn-COF presents high crystallinity in the PXRD test (Fig. 1b and Fig. S1 online). A negligible difference (R_{p} , 2.51% and R_{wp} , 3.19%) has been detected in the Pawley refinements reproduced results when compared with the experimentally detected PXRD pattern (Fig. 1b). AAn-COF exhibits high crystallinity and a series of peaks at 4.1° , 7.1° , 8.2° , 10.8° , 12.2° and 26.8° are assigned to (100), (2 - 1 0), (200), (3 - 1 0), (300) and (001) crystal faces, respectively (Fig. 1b and Fig. S1 online). The results comply with the $P6/m$ space group that possessed 2D hexagonal layered network and eclipsed AA stacking mode (Fig. S1b online). In addition, FT-IR and ^{13}C NMR measurements have been conducted to prove the structure of AAn-COF. In the FT-IR spectra, AAn-COF as a kind of β -ketoenamine-linked COFs has no stretching bands of imine (C=N) groups owing to the existence of tautomerism effect, in which the enol form can transform into keto form (Fig. S2 online) [41–43]. Instead, strong C=C ($\sim 1568 \text{ cm}^{-1}$) and C-N ($\sim 1265 \text{ cm}^{-1}$) stretching bands that are ascribed to keto form have been detected. Besides, the C=O peak merges with the C=C stretching vibration accompanied with the diminishing of C=O of TP, which might be ascribed the extended conjugation and hydrogen bonding interaction (Fig. S2 online). The ^{13}C NMR spectra of AAn-COF display characteristic signal of C=O bond (182.7 ppm) and C-N bond (~ 144 ppm) for β -ketoenamine-linked AAn-COF, which further confirms the successful formation of AAn-COF (Fig. 1c). Based on the above results of AAn-COF, OH-AAn-COF with close construction units has been studied except that AAn is replaced with OH-AAn. OH-AAn-COF displays peak signals at 4.1° , 7.1° , 8.1° , 10.8° , 13.6° and a broad peak at 27.1° , which can be assigned to the $P6/m$ space group that represented similar structure as that of AAn-COF (Fig. S3 online) [41]. The FT-IR and ^{13}C NMR spectra for OH-AAn-COF are close to that of AAn-COF with slight difference in peak position and intensity (Figs. S4 and S5 online).

Post-modification of AAn-COF and OH-AAn-COF are prepared through metalation of COFs with a heat-assisted reflux method. After treatment, the PXRD patterns comply with the pristine ones, confirming the retention of COFs structures (Figs. S6–S8 online). The FT-IR spectra of AAn-COF-M (M = Cu, Co, and Zn) are close to that of AAn-COF (Figs. S2 and S9 online). Furthermore, XPS tests show that the detected Cu $2p_{3/2}$ binding energy of 934.1 eV and $2p_{1/2}$ binding energy of 953.7 eV in AAn-COF-Cu are consistent with Cu (II) (Figs. S10 and S11 online). For AAn-COF-Co and AAn-COF-Zn, the binding energy of Co $2p_{3/2}$ at 781.8 eV and Zn $2p_{3/2}$ at 1022.2 eV are ascribed to Co (II) and Zn (II), respectively (Figs. S12–S14 online). Besides, the difference in the binding energy of AAn-COF-M and relative metal acetates has been studied to validate the interaction between metal ions and COFs. For example, the Cu $2p_{3/2}$ binding energy in AAn-COF-Cu is 934.1 eV and the value for copper acetate is 935.1 eV, which is possibly due to the coordinated carbonyl group in COFs that might change the electron cloud density of Cu species (Fig. S15 online) [44–46]. Besides, the PXRD and FT-IR tests of OH-AAn-COF-Cu are close to that of OH-AAn-COF (Figs. S7 and S16 online). In addition, the XPS results of OH-AAn-COF-Cu display similar results when compared with that

of AAn-COF-Cu, which prove the successful modification of transition metals (Figs. S10 and S17 online).

For AAn-COF and OH-AAn-COF, the generated porous 2D layered structures would facilitate the mass transfer and CO₂ enrichment. Thus, the N₂ and CO₂ sorption tests have been conducted. Taking AAn-COF and AAn-COF-Cu for example, the Brunner-Emmet-Teller surface area (S_{BET}) of AAn-COF-Cu is measured to be 161 m² g⁻¹, which is lower than that of AAn-COF (S_{BET} , 237 m² g⁻¹) without metal doping (Fig. 1d and Fig. S18 online). Furthermore, the CO₂ adsorption capacity of AAn-COF and AAn-COF-Cu are measured to be 49 and 24 cm³ g⁻¹ at 298 K, respectively (Fig. S19 online). Similarly, the S_{BET} of OH-AAn-COF-Cu (470 m² g⁻¹) is also lower than that of OH-AAn-COF (S_{BET} , 535 m² g⁻¹) without metal doping (Figs. S20 and S21 online). Besides, the CO₂ adsorption capacity presents similar trends for OH-AAn-COF (25 cm³ g⁻¹, 298 K) and OH-AAn-COF-Cu (17 cm³ g⁻¹, 298 K) when compared with those of AAn-COF and AAn-COF-Cu (Fig. S22 online).

To characterize the morphology of the obtained samples, SEM and TEM tests are further conducted. Taking AAn-COF-Cu for instance, the SEM test shows that it displays nanofiber morphology (denoted as AAn-COF-Cu (NF)) with average diameter of ~40 nm and length of ~0.5 μm, which is similar to AAn-COF without Cu doping (Fig. S23 online). The nanofiber morphology is also verified by the TEM test (Fig. 2a). Moreover, the high-resolution TEM (HR-TEM) shows that AAn-COF-Cu (NF) presents ordered pore channels, which comply with the simulated pore structure of AAn-COF-Cu (Fig. 2b). Elemental mapping test reveals that C, N, O and Cu are uniformly distributed in AAn-COF-Cu (NF) (Fig. 2c). The total Cu content in AAn-COF-Cu (NF) is determined to be 8.40 wt% by ICP-OES test (Table S1 online). Moreover, AAn-COF-M (M = Co and Zn) display similar morphology as that of AAn-COF-Cu (NF) (Figs. S24 and S25 online). In contrast, OH-AAn-COF-Cu presents hollow tube morphology (denoted as OH-AAn-COF-Cu (HT)) with an outer diameter size of ~200 nm in the SEM image, which is similar to OH-AAn-COF (HT) (Fig. S26 online). Besides, the average length of OH-AAn-COF-Cu (HT) is ~1 μm with a wall thickness of ~18 nm. The hollow tube morphology is further certified by the

TEM test (Fig. 2d). In addition, HR-TEM image of OH-AAn-COF-Cu (HT) presents ordered pore channels, which also complies with the pore structure of OH-AAn-COF-Cu (HT) (Fig. 2e). EDS mapping image reveals that C, N, O and Cu are uniformly distributed in OH-AAn-COF-Cu (HT) (Fig. 2f). Moreover, to estimate the Cu content of OH-AAn-COF-Cu, we have added a detailed ICP-OES test and the result shows that Cu content in OH-AAn-COF-Cu (NF) is 9.38 wt% (Table S1 online).

With two kinds of different COF-based morphologies in hand, we further set out to explore the possible formation mechanism with the support of phase and morphology characterization at various reaction time. Taking AAn-COF (NF) as an example, the precursors are mixed and added into several heat-resistant glass tubes and reacted for different time (1 to 72 h). The obtained crystallinity and morphology of samples with different reaction time are studied by PXRD and SEM tests. The PXRD tests clearly reflect the process of crystallinity transition from amorphous to highly crystalline with the increase of reaction time, during which the peak of AAn-COF (NF) starts to appear at 3 h and gradually become stronger in intensity during the process that time prolongs to 72 h (Fig. S27a online). As revealed by the SEM images, the oligomer is agglomerated to generate small nanoparticles (diameter, ~45 nm) after 1 h and the small nanoparticles become larger (diameter, ~52 nm) after 3 h (Fig. S28 online). At 6 h, the nanoparticles are stacked to produce a kind of nanosheets (diameter, ~200 nm) (Fig. 3a). Then, the nanosheets become larger in size and nanofibers (diameter, ~12 nm) start to generate on their surface at 12 h (Fig. 3b). From 12 to 24 h, the nanofibers become thicker and all of the nanosheets gradually transfer into uniform nanofibers (diameter, ~35 nm) (Fig. 3c and Fig. S28 online). After that, the surface of nanofibers becomes rough and a kind of mace-like nanofibers (~40 nm) are formed at 72 h (Fig. 3d and Fig. S28 online). Based on the above results from PXRD and SEM tests, the formation process of nanofibers follows a kind of nanosheet based self-template mechanism [35,36], which has been rarely reported in “bottom-up” strategies. In detail, the condensation reaction between the monomers is uniformly nucleated to rapidly generate small nanoparticles, which are quickly piled up to produce nanosheets

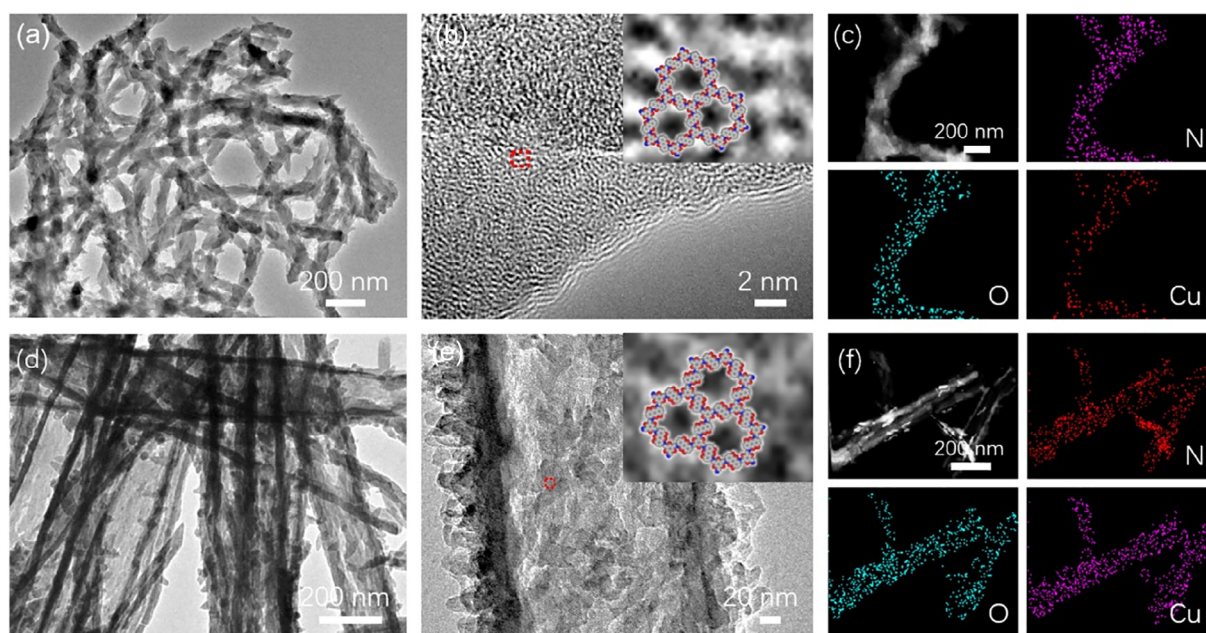


Fig. 2. (Color online) The morphology characterization of AAn-COF-Cu (NF) and OH-AAn-COF-Cu (HT). (a) TEM image of AAn-COF-Cu (NF). (b) HR-TEM image of AAn-COF-Cu (NF) (inset is the pore structure image). (c) Elemental mapping image of AAn-COF-Cu (NF). (d) TEM image of OH-AAn-COF-Cu (HT). (e) HR-TEM image of OH-AAn-COF-Cu (HT) (inset is the pore structure image). (f) Elemental mapping image of OH-AAn-COF-Cu (HT).

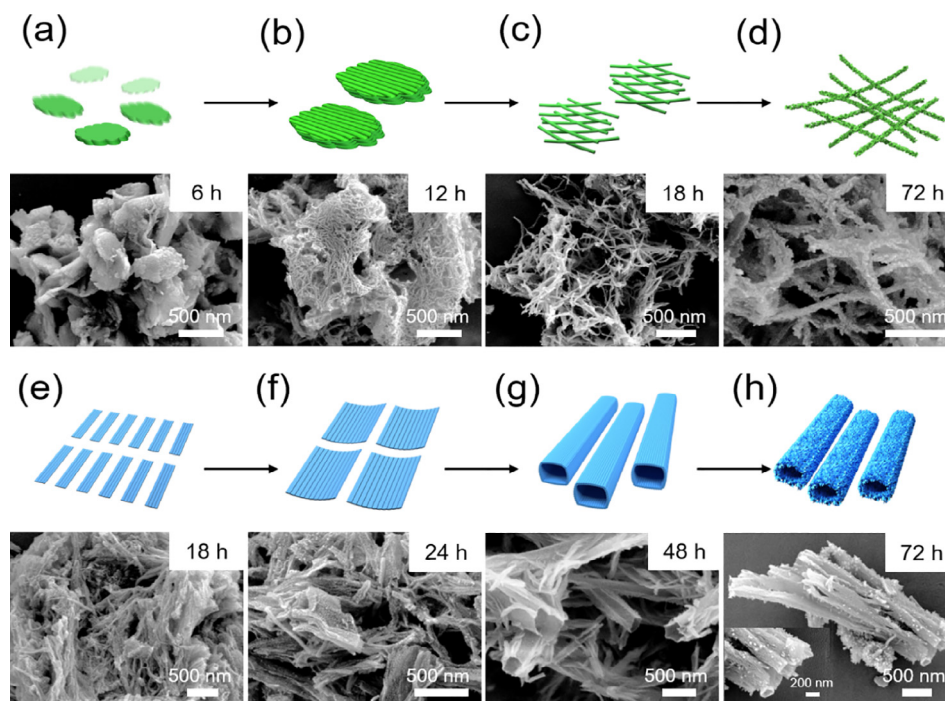


Fig. 3. (Color online) The schematic representation and SEM images of AAn-COF and OH-AAn-COF obtained from different reaction time. (a–d) Schematic representation and SEM images of AAn-COF (NF) at 6, 12, 18 and 72 h. (e–h) Schematic representation and SEM images of OH-AAn-COF (HT) at 18, 24, 48 and 72 h.

at the early stage. Then, the nanosheets become larger and gradually transform into 1D nanofibers under the effect of continuously reversible polymerization/crystallization due to the unique and dynamic imine bonds [31,37]. Finally, the nanosheets completely transform into nanofibers and gradually become longer and rougher with the increase of reaction time.

As a comparison, we further study the formation process of hollow tube morphology of OH-AAn-COF (HT) at different reaction time. Similarly, SEM and PXRD tests have been performed to evaluate the process. As shown in the PXRD tests, the peaks of OH-AAn-COF (HT) start to appear at 18 h (Fig. S27b online). After that, the peak intensity increases from 18 to 72 h, implying OH-AAn-COF (HT) is gradually transformed into higher crystalline states (Fig. S27b online). Therefore, the reaction time for the SEM test is selected from 18 to 72 h. The SEM image shows that OH-AAn-COF displays aggregated small nanobelt morphology at 18 h (Fig. 3e). Then, these small nanobelts are self-assembled to produce partially curled nanosheets at 24 h (Fig. 3f). After that, the curled nanosheets are rolled to generate hollow tubes (outer diameter, ~200 nm and wall thickness, ~15 nm) after 48 h (Fig. 3g). Finally, the morphology can be well-regulated to be uniform hollow tubes along the time and hollow tubes (outer diameter, ~200 nm and wall thickness, ~18 nm) with relative rough surface can be obtained at 72 h (Fig. 3h). Based on the results from PXRD and SEM tests, the formation process of hollow tubes follows the nanosheet-crimping mechanism, and this is the second example of COF-based hollow tubes that follows this mechanism as far as we know [34]. As shown in the above-mentioned results, OH-AAn-COF and AAn-COF have iso-reticular structures yet display drastically different morphologies. The possible reason is proposed based on the above results as follows: (1) the introduction of hydroxyl group will affect the crystallization and morphology formation processes of OH-AAn-COF (HT) when compared with that of AAn-COF (NF) as certified by the PXRD and SEM tests; (2) the initial formation processes of COFs are mainly controlled by kinetics process, involving the assembly of thermodynamically unstable

small nanoparticles or nanobelts that self-assembly into larger ones, which will serve as vital precursors or templates for the formation of different morphologies [32,47] and (3) OH-AAn-COF (HT) with a large amount of hydroxyl group might provide additional hydrogen bonds, which would induce the nanosheet-crimping process and assemble into hollow tubes rather than nanofibers. Based on the above results and discussion, we have successfully obtained anthraquinone COF-based 1D superstructures with different morphologies and explored their possible formation mechanisms, which will provide sufficient models for further investigation.

Stability is an essential factor in studying the durability of catalysts under various conditions [48]. To evaluate the thermal stability, thermogravimetric analysis (TGA) tests have been performed under air atmosphere. Taking AAn-COF-Cu (NF) as an example, it exhibits high thermal stability with slight weight loss up to ~350 °C, which complies with the result of AAn-COF (NF) (Fig. S29 online). Moreover, to investigate the chemical stability of AAn-COF-M (M = Cu, Co, and Zn) and OH-AAn-COF-Cu, the samples are soaking in 1 mol L⁻¹ KOH for more than 24 h. The PXRD pattern of AAn-COF-Cu (NF) shows remained peaks when compared with the simulated one (Fig. S30a online). Similar results are also detected for AAn-COF-M (M = Co and Zn) and OH-AAn-COF-Cu (Figs. S30b and S31 online). The high stability of AAn-COF-M (M = Cu, Co and Zn) and OH-AAn-COF-Cu set basis for electrocatalytic CO₂RR applications.

3.2. The electrocatalytic performance of samples

The linear sweep voltammetry (LSV) curves show that AAn-COF-Cu (NF) has a total current density of $-379.7 \text{ mA cm}^{-2}$ at -1.1 V , which is higher than that of OH-AAn-COF-Cu (HT) ($-311.2 \text{ mA cm}^{-2}$) (Fig. 4a). Besides, AAn-COF-Cu (NF) shows a much smaller current density in hydrogen evolution reaction (HER) than that in CO₂RR, implying it strongly favors CO₂RR than HER (Fig. S32 online). To evaluate the reduction product of CO₂RR,

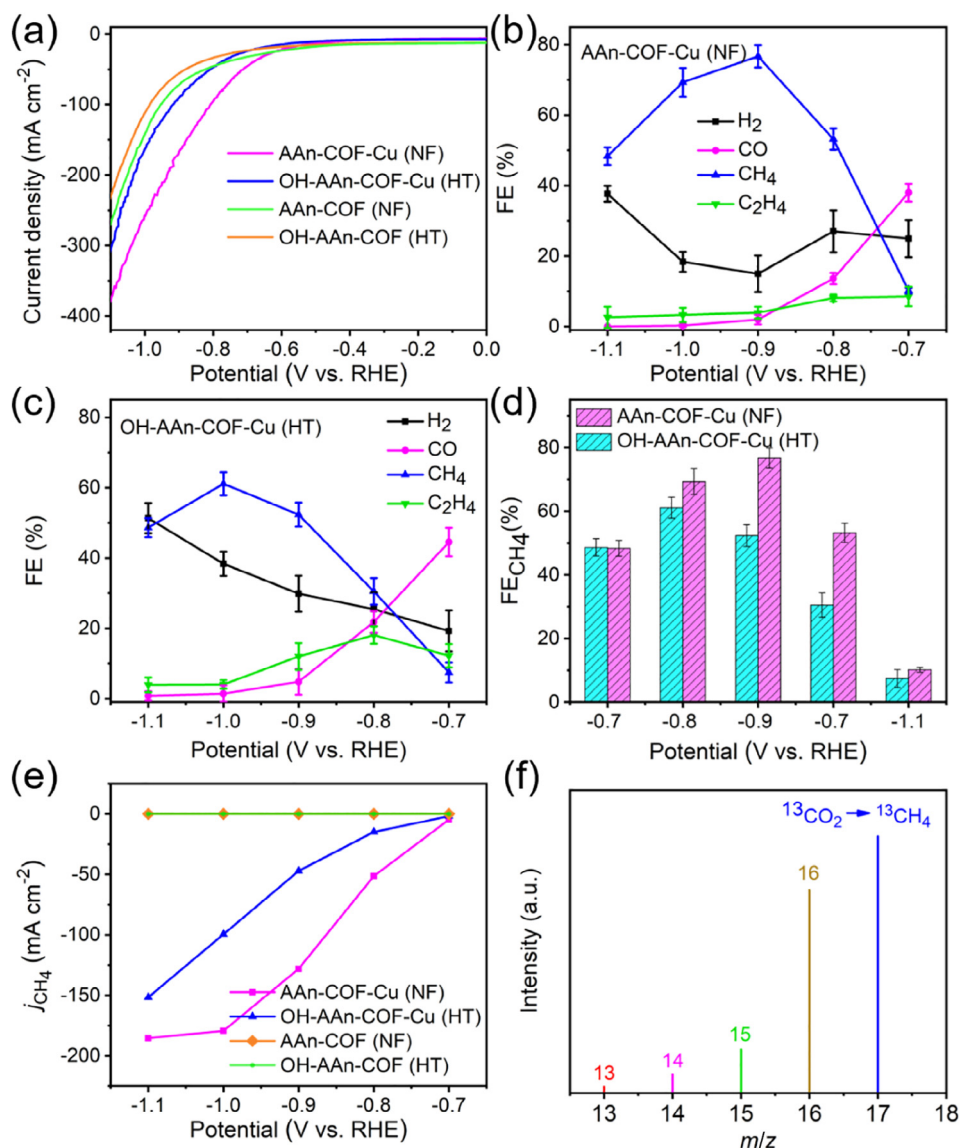


Fig. 4. (Color online) Electrochemical performance of AAn-COF-Cu (NF) and OH-AAn-COF-Cu (HT). (a) Linear sweep voltametric curves. (b) Faradaic efficiencies of AAn-COF-Cu (NF) at different applied potentials. (c) Faradaic efficiencies of OH-AAn-COF-Cu (HT) at different applied potentials. (d) Faradaic efficiencies for CH₄ at different applied potentials. (e) Partial CH₄ current density. (f) The mass spectra of ¹³CH₄ recorded under ¹³CO₂ atmosphere.

electrocatalysis reactions are carried out at different potentials and the reduction products are detected by GC and ¹H NMR tests (Figs S33, S34 online). As a result, CH₄ is found to be the dominant product and there is no liquid product for both AAn-COF-Cu (NF) and OH-AAn-COF-Cu (HT). In contrast, the electroreduction products for samples without metal doping or carbon paper are mainly H₂ (Fig. S34 online). For AAn-COF-Cu (NF), it gives a FE_{CH₄} of 10% at -0.7 V and a FE_{C₂H₄} of 9% with a current density of -45.3 mA cm⁻² (Fig. S32 online). With the increase of potential, the FE_{CH₄} enhances to 77% at -0.9 V while FE_{C₂H₄} remains almost unchanged (<10%). The FE_{CH₄} of AAn-COF-Cu (NF) keeps higher than 53% in a wide potential range (-0.8 to -1.0 V) (Fig. 4b and d). The dominant products for most of the reported crystalline COFs are CO and CH₄ has been rarely reported [23,24,28]. Noteworthy, the maximum FE_{CH₄} value (77%, -0.9 V) of AAn-COF-Cu (NF) in this work is the highest among reported crystalline COFs and superior to most of Cu-based electrocatalysts (Fig. 5c and Table S2 online) [23,24,49]. In contrast, OH-AAn-COF-Cu (HT) gives the highest FE_{CH₄} of only 61% at -1.0 V (Fig. 4c, 4d and Fig. S35 online). Specif-

ically, the highest FE_{C₂H₄} of OH-AAn-COF-Cu (HT) is almost doubly increased (19%, -0.8 V) when compared with that of AAn-COF-Cu (NF) (9%, -0.7 V), which might be attributed to the tuning effect of the hollow structure that are beneficial for the C-C coupling in the PCET process (Fig. 4b, c) [50,51].

To further support the activity of AAn-COF-Cu (NF), partial current densities of CH₄, CO, C₂H₄, and H₂ are calculated (Fig. 4d and Fig. S32 online). AAn-COF-Cu (NF) gives a partial CH₄ current density of -128.1 mA cm⁻² at -0.9 V, which is almost three times than that of OH-AAn-COF-Cu (HT) (-47.1 mA cm⁻²) (Fig. 4e). Besides, an isotopic experiment that applying ¹³CO₂ has been performed to reveal the carbon source. As shown in Fig. 4f and Fig. S36 (online), the peaks at *m/z* = 17, 29 and 30 are assigned to ¹³CH₄, ¹³CO, and ¹³C₂H₄, respectively, indicating the carbon sources of CH₄, CO, and C₂H₄ indeed derive from the CO₂ used.

To test the electrochemical active surface area (ECSA), electrochemical double-layer capacitance (*C_{dl}*) is analyzed (Fig. 5a and Fig. S37 online). The results show that AAn-COF-Cu (NF) exhibits a *C_{dl}* value of 1.18 mF cm⁻², which is larger than that of OH-

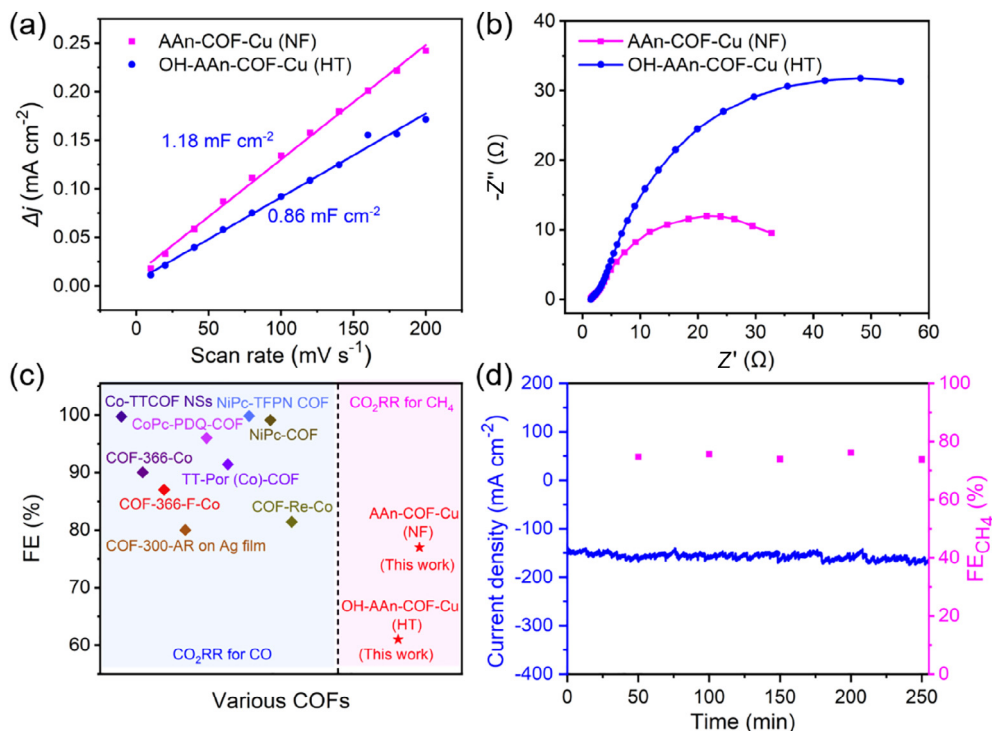


Fig. 5. (Color online) Electrochemical performance of AAn-COF-Cu (NF) and OH-AAn-COF-Cu (HT). (a) Capacitive current at 0.05 V as a function of scan rate for AAn-COF-Cu (NF) and OH-AAn-COF-Cu (HT). (b) Nyquist plots of AAn-COF-Cu (NF) and OH-AAn-COF-Cu (HT). (c) The summary of CO₂RR performance for reported COFs based electrocatalysts. (d) Long time durability test of AAn-COF-Cu (NF) at the potential of -0.9 V vs. RHE.

AAn-COF-Cu (HT) (0.86 mF cm^{-2}). Besides, the charge transfer resistance of AAn-COF-Cu (NF) and OH-AAn-COF-Cu (HT) are calculated to be 38.69 and 78.96Ω , respectively, which suggests that NF might be more favorable for electron transfer than HT (Fig. 5b and Fig. S38 online).

To reveal the superiority of AAn-COF-Cu (NF), AAn-COF-Co (NF) and AAn-COF-Zn (NF) are prepared and tested. As a result, CO and H₂ are the dominant products for AAn-COF-Zn (NF) and the highest FE_{CO} is 78% at -0.7 V (Fig. S39 online). With the increase of potential, the FE_{CO} gradually decreases and finally results in dominant product of H₂. In contrast, AAn-COF-Co has no CO₂ reduction performance at all selected potentials (Fig. S40 online). Besides, the C_{dl} values of AAn-COF-Zn (NF) and AAn-COF-Co (NF) are calculated to be 0.88 and 0.84 mF cm^{-2} , respectively (Fig. S41 online).

In addition, the long-time durability test has been carried out at -0.9 V by chronoamperometric curves to evaluate the electrochemical stability of AAn-COF-Cu (NF) (Fig. 5d). After 250 min, AAn-COF-Cu (NF) performs negligible decay in activity and FE_{CH₄} when compared with the initial one. During the process, the corresponding FE_{CH₄} can be maintained higher than 73.8% and the current density remains at about -166 mA cm^{-2} over the entire experiment (Fig. 5d). After the test, the PXRD patterns show remained peaks of AAn-COF-Cu (NF) and OH-AAn-COF-Cu (HT) when compared with samples before reactions, indicating high stability during the electrochemical CO₂RR process (Figs. S42 and S43 online).

4. Conclusion

In summary, we have designed two kinds of anthraquinone-based COFs with tunable 1D superstructures (e.g., nanofibers and hollow tubes) via Schiff-base condensation reaction and explored their 1D morphology formation-mechanism. Interestingly, a rarely reported nanosheet-based self-template mechanism and a

nanosheet-crimping mechanism have been demonstrated for the production of COF-based nanofibers and hollow tubes, respectively, as supported by sufficient time-interval experiments. The obtained COF-based superstructures possess a large surface area, high stability, CO₂ enrichment/activation properties, and can be post-modified with transition metals for efficient CO₂RR to CH₄. Specifically, AAn-COF-Cu (NF) and OH-AAn-COF-Cu (HT) exhibit excellent FE_{CH₄} of 77% ($-128.1 \text{ mA cm}^{-2}$, -0.9 V) and 61% (-99.5 mA cm^{-2} , -1.0 V) in a flow cell, respectively. Noteworthy, the FE_{CH₄} of AAn-COF-Cu (NF) is higher than 53% over a wide potential range (-0.8 to -1.0 V) and the achieved FE_{CH₄} of 77% (-0.9 V) is the highest one among reported crystalline COFs. This is the first example of anthraquinone-based COFs with well-tuned 1D superstructures that can be applied in efficient electrocatalytic CO₂RR to CH₄, which would promote the exploration of morphology-controlled COFs in this field.

Conflict of interest

The authors declare that they have no conflict of interest.

Acknowledgments

This work was supported by the National Natural Science Foundation of China (21871141, 21871142, 21901122, 22071109 and 92061101), the Natural Science Research of Jiangsu Higher Education Institutions of China (19KJB150011), China Postdoctoral Science Foundation (2018M630572 and 2019M651873), Postgraduate Research & Practice Innovation Program of Jiangsu Province (KYCX20_1171), Priority Academic Program Development of Jiangsu Higher Education Institutions and the Foundation of Jiangsu Collaborative Innovation Center of Biomedical Functional Materials.

Author contributions

Ya-Qian Lan, Yifa Chen and Ming Liu conceived and designed the idea. Ming Liu, Yi-Rong Wang and Hui-Min Ding designed the experiments, collected and analyzed the data. Guang-Kuo Gao, Long-Zhang Dong, Qi Li and Shun-Li Li assisted with the experiments and characterizations. Ming Liu and Yi-Rong Wang wrote the manuscript. Ya-Qian Lan, Yifa Chen and Ming Liu discussed the results and prepared the manuscript. All the authors reviewed and contributed to this paper.

Appendix A. Supplementary materials

Supplementary materials to this article can be found online at <https://doi.org/10.1016/j.scib.2021.05.001>.

References

- Diercks CS, Yaghi OM. The atom, the molecule, and the covalent organic framework. *Science* 2017;355:eaal1585.
- Côté AP, Benin AI, Ockwig NW, et al. Porous, crystalline, covalent organic frameworks. *Science* 2005;310:1166–70.
- DeBlase CR, Silberstein KE, Truong T-T, et al. β -ketoenamine-linked covalent organic frameworks capable of pseudocapacitive energy storage. *J Am Chem Soc* 2013;135:16821–4.
- Fan H, Mundstock A, Feldhoff A, et al. Covalent organic framework-covalent organic framework bilayer membranes for highly selective gas separation. *J Am Chem Soc* 2018;140:10094–8.
- Wang Z, Zhang S, Chen Y, et al. Covalent organic frameworks for separation applications. *Chem Soc Rev* 2020;49:708–35.
- Wu X, Hong Y-L, Xu B, et al. Perfluoroalkyl-functionalized covalent organic frameworks with superhydrophobicity for anhydrous proton conduction. *J Am Chem Soc* 2020;142:14357–64.
- Tao S, Zhai L, Dinga Wonanke AD, et al. Confining H_3PO_4 network in covalent organic frameworks enables proton super flow. *Nat Commun* 2020;11.
- Jhulki S, Evans AM, Hao X-L, et al. Humidity sensing through reversible isomerization of a covalent organic framework. *J Am Chem Soc* 2020;142:783–91.
- Dong J, Zhang K, Li X, et al. Ultrathin two-dimensional porous organic nanosheets with molecular rotors for chemical sensing. *Nat Commun* 2017;8:1142.
- Mitra S, Sasmal HS, Kundu T, et al. Targeted drug delivery in covalent organic nanosheets (CONs) via sequential postsynthetic modification. *J Am Chem Soc* 2017;139:4513–20.
- Zhong W, Sa R, Li L, et al. A covalent organic framework bearing single ni sites as a synergistic photocatalyst for selective photoreduction of CO_2 to CO. *J Am Chem Soc* 2019;141:7615–21.
- Haug WK, Wolfson ER, Morman BT, et al. A nickel-doped dehydrobenzoannulene-based two-dimensional covalent organic framework for the reductive cleavage of inert aryl C-S bonds. *J Am Chem Soc* 2020;142:5521–5.
- Cui X, Lei S, Wang AC, et al. Emerging covalent organic frameworks tailored materials for electrocatalysis. *Nano Energy* 2020;70:104525.
- Wang Y, Chen J, Wang G, et al. Perfluorinated covalent triazine framework derived hybrids for the highly selective electroconversion of carbon dioxide into methane. *Angew Chem Int Ed* 2018;57:13120–4.
- Liu R, Tan KT, Gong Y, et al. Covalent organic frameworks: an ideal platform for designing ordered materials and advanced applications. *Chem Soc Rev* 2021;50:120–242.
- Li X, Yadav P, Loh KP. Function-oriented synthesis of two-dimensional (2D) covalent organic frameworks - from 3D solids to 2D sheets. *Chem Soc Rev* 2020;49:4835–66.
- Rogge SMJ, Bavykina A, Hajek J, et al. Metal-organic and covalent organic frameworks as single-site catalysts. *Chem Soc Rev* 2017;46:3134–84.
- Wang Y-R, Yang R-X, Chen Y, et al. Chloroplast-like porous bismuth-based core-shell structure for high energy efficiency CO_2 electroreduction. *Sci Bull* 2020;65:1635–42.
- Huang N, Lee KH, Yue Y, et al. A stable and conductive metallophthalocyanine framework for electrocatalytic carbon dioxide reduction in water. *Angew Chem Int Ed* 2020;59:16587–93.
- Diercks CS, Lin S, Kormienko N, et al. Reticular electronic tuning of porphyrin active sites in covalent organic frameworks for electrocatalytic carbon dioxide reduction. *J Am Chem Soc* 2018;140:1116–22.
- Zhu H-J, Lu M, Wang Y-R, et al. Efficient electron transmission in covalent organic framework nanosheets for highly active electrocatalytic carbon dioxide reduction. *Nat Commun* 2020;11:497.
- Lin S, Diercks CS, Zhang Y-B, et al. Covalent organic frameworks comprising cobalt porphyrins for catalytic CO_2 reduction in water. *Science* 2015;349:1208–13.
- Wu Q, Mao M-J, Wu Q-J, et al. Construction of donor-acceptor heterojunctions in covalent organic framework for enhanced CO_2 electroreduction. *Small* 2020. <https://doi.org/10.1002/smll.202004933>.
- Zhang M-D, Si D-H, Yi J-D, et al. Conductive phthalocyanine-based covalent organic framework for highly efficient electroreduction of carbon dioxide. *Small* 2020. <https://doi.org/10.1002/smll.202005254>.
- Liu H, Chu J, Yin Z, et al. Covalent organic frameworks linked by amine bonding for concerted electrochemical reduction of CO_2 . *Chem* 2018;4:1696–709.
- Li J, Jing X, Li Q, et al. Bulk COFs and COF nanosheets for electrochemical energy storage and conversion. *Chem Soc Rev* 2020;49:3565–604.
- Ye K, Cao A, Shao JQ, et al. Synergy effects on Sn-Cu alloy catalyst for efficient CO_2 electroreduction to formate with high mass activity. *Sci Bull* 2020;65:711–9.
- Rodríguez-San-Miguel D, Montoro C, Zamora F. Covalent organic framework nanosheets: preparation, properties and applications. *Chem Soc Rev* 2020;49:2291–302.
- Wang S, Wang Q, Shao P, et al. Exfoliation of covalent organic frameworks into few-layer redox-active nanosheets as cathode materials for lithium-ion batteries. *J Am Chem Soc* 2017;139:4258–61.
- Peng Y, Huang Y, Zhu Y, et al. Ultrathin two-dimensional covalent organic framework nanosheets: preparation and application in highly sensitive and selective DNA detection. *J Am Chem Soc* 2017;139:8698–704.
- Pachfule P, Kandambeth S, Mallick A, et al. Hollow tubular porous covalent organic framework (COF) nanostructures. *Chem Commun* 2015;51:11717–20.
- Zhang F, Wei S, Wei W, et al. Trimethyltriazine-derived olefin-linked covalent organic framework with ultralong nanofibers. *Sci Bull* 2020;65:1659–66.
- Yan Y, Lu Y, Wang B, et al. Self-assembling hydrophilic magnetic covalent organic framework nanospheres as a novel matrix for phthalate ester recognition. *ACS Appl Mater Interfaces* 2018;10:26539–45.
- Gole B, Stepanenko V, Rager S, et al. Microtubular self-assembly of covalent organic frameworks. *Angew Chem Int Ed* 2018;57:846–50.
- Kandambeth S, Venkatesh V, Shinde DB, et al. Self-templated chemically stable hollow spherical covalent organic framework. *Nat Commun* 2015;6:6786.
- Liu Y-Y, Li X-C, Wang S, et al. Self-templated synthesis of uniform hollow spheres based on highly conjugated three-dimensional covalent organic frameworks. *Nat Commun* 2020;11:5561.
- El-Mahdy AFM, Young C, Kim J, et al. Hollow microspherical and microtubular [3 + 3] carbazole-based covalent organic frameworks and their gas and energy storage applications. *ACS Appl Mater Interfaces* 2019;11:9343–54.
- Das G, Skorjanc T, Sharma SK, et al. Viologen-based conjugated covalent organic networks via zinc reaction. *J Am Chem Soc* 2017;139:9558–65.
- Huang W, Jiang Y, Li X, et al. Solvothermal synthesis of microporous, crystalline covalent organic framework nanofibers and their colorimetric nanohybrid structures. *ACS Appl Mater Interfaces* 2013;5:8845–9.
- Gu S, Wu S, Cao L, et al. Tunable redox chemistry and stability of radical intermediates in 2D covalent organic frameworks for high performance sodium ion batteries. *J Am Chem Soc* 2019;141:9623–8.
- Dong B, Wang W-J, Pan W, et al. Ionic liquid as a green solvent for ionothermal synthesis of 2D keto-enamine-linked covalent organic frameworks. *Mater Chem Phys* 2019;226:244–9.
- Biswal BP, Chandra S, Kandambeth S, et al. Mechanochemical synthesis of chemically stable isoreticular covalent organic frameworks. *J Am Chem Soc* 2013;135:5328–31.
- Chandra S, Kundu T, Dey K, et al. Interplaying intrinsic and extrinsic proton conductivities in covalent organic frameworks. *Chem Mater* 2016;28:1489–94.
- Han X, Zhang J, Huang J, et al. Chiral induction in covalent organic frameworks. *Nat Commun* 2018;9:1294.
- Lu X, Jiang Z, Yuan X, et al. A bio-inspired O_2 -tolerant catalytic CO_2 reduction electrode. *Sci Bull* 2019;64:1890–5.
- Lu M, Li Q, Liu J, et al. Installing earth-abundant metal active centers to covalent organic frameworks for efficient heterogeneous photocatalytic CO_2 reduction. *Appl Catal B* 2019;254:624–33.
- Ma W, Zheng Q, He Y, et al. Size-controllable synthesis of uniform spherical covalent organic frameworks at room temperature for highly efficient and selective enrichment of hydrophobic peptides. *J Am Chem Soc* 2019;141:18271–7.
- Guan X, Li H, Ma Y, et al. Chemically stable polyarylether-based covalent organic frameworks. *Nat Chem* 2019;11:587–94.
- Yusran Y, Fang Q, Valtchev V. Electroactive covalent organic frameworks: design, synthesis, and applications. *Adv Mater* 2020;32:2002038.
- Yang P-P, Zhang X-L, Gao F-Y, et al. Protecting copper oxidation state via intermediate confinement for selective CO_2 electroreduction to C_2+ fuels. *J Am Chem Soc* 2020;142:6400–8.
- Fan L, Xia C, Yang F, et al. Strategies in catalysts and electrolyzer design for electrochemical CO_2 reduction toward C_2+ products. *Sci Adv* 2020;6:eaay3111.



Ming Liu received his B.S. degree (2018) in Harbin University of Science and Technology, and now he is studying for a master's degree at Nanjing Normal University. At present, his research focuses on the design and synthesis of highly efficient COF-based hybrid catalysts.



Yifa Chen received his B.S. degree from School of Chemistry, Beijing Institute of Technology. He subsequently obtained his Ph.D. degree from School of Chemistry and Chemical Engineering, Beijing Institute of Technology under the supervision of Prof. Bo Wang. In 2018, he joined Prof. Ya-Qian Lan's group as an associate professor at College of Chemistry and Materials Science of Nanjing Normal University. His research interest focuses on the fabrication of MOF-based devices like membranes, foams and fibers that can be applicable in energy storage and conversion, proton conductivity or photo/electric heterogeneous catalysis.



Yi-Rong Wang received her B.S. degree (2016) and M.S. degree (2019) from Harbin Normal University and Nanjing Normal University, respectively, and now she is studying for Ph.D. degree at Nanjing Normal University. Her current research focuses on the synthesizing of metal-organic framework (MOF)-based hybrid electrocatalysts for electrocatalytic reduction of carbon dioxide.



Ya-Qian Lan received his B.S. and Ph.D. degrees (2009) from Northeast Normal University under the supervision of Prof. Zhong-Min Su. In 2010, he joined Prof. Qiang Xu's group at National Institute of Advanced Industrial Science and Technology (AIST, Japan) as a JSPS postdoctoral fellow. Since 2012, he has been a Professor of Chemistry at Nanjing Normal University. His current research interest focuses on applying polyoxometalate-based composite materials in energy storage and conversion and porous metal-organic frameworks for applications in catalysis and proton conduction.



Hui-Min Ding received her B.S. degree (2020) from Shandong Liaocheng University, and now she is studying for a master's degree at Nanjing Normal University. At present, her research focuses on the design and synthesis of highly efficient MOF-based hybrid electrocatalysts for electrocatalytic reduction of carbon dioxide.